

Next-to-leading order QCD predictions for $A^0\gamma$ associated production at the CERN Large Hadron Collider

Liang Dai,¹ Ding Yu Shao,¹ Chong Sheng Li,^{1,2,*} Jun Gao,¹ and Hao Zhang¹

¹*Department of Physics and State Key Laboratory of Nuclear Physics and Technology,
Peking University, Beijing 100871, China*

²*Center for High Energy Physics, Peking University, Beijing 100871, China*

(Dated: May 15, 2022)

Abstract

We calculate the complete next-to-leading-order (NLO) QCD corrections (including SUSY QCD corrections) to the inclusive total cross sections of the associated production processes $pp \rightarrow A^0\gamma + X$ in the minimal supersymmetric standard model (MSSM) at the CERN Large Hadron Collider (LHC). Our results show that the enhancement of the total cross sections from the NLO QCD corrections can reach 25% \sim 15% for $200 \text{ GeV} < m_A < 500 \text{ GeV}$ and $\tan\beta = 50$. The scale dependence of the total cross section is improved by the NLO corrections in general. We also show the Monte Carlo simulation results for the $\tau^+\tau^- + \gamma$ signature including the complete NLO QCD effects, and find an observable signature above the standard model (SM) background for a normal luminosity of 100 fb^{-1} at the LHC.

PACS numbers: 12.38.Bx, 12.60.Jv, 14.80.Da

*Electronic address: csli@pku.edu.cn

I. INTRODUCTION

Electroweak symmetry breaking (EWSB) plays a key role in the current research of elementary particles. However, the experimental effort to validate the Higgs mechanism on the CERN Large Hadron Collider (LHC) with a center of mass energy $\sqrt{s} = 14$ TeV and a luminosity of 100 fb^{-1} per year [1], is a great challenge. In the standard model (SM) of particle physics, there is only one Higgs particle, which is expected to be lurking somewhere close to the experimental lower bound of 114.4 GeV set by LEP2 [2]. In the minimal supersymmetric standard model (MSSM), two complex Higgs doublets are introduced to eliminate gauge anomaly [3], resulting in two CP-even (h^0, H^0) and one CP-odd (A^0) neutral Higgs bosons, as well as a pair of charged Higgs bosons. The Higgs sector of the MSSM, at leading order, is characterized by two parameters: one is m_A the mass of the pseudo-scalar Higgs boson, and the other $\tan\beta$ the ratio of up- and down-Higgs doublet vacuum expectation value (VEV). Particularly, current experiments hint a scenario with large $\tan\beta \gtrsim 45$ and thus large couplings between the pseudo-scalar Higgs and down-type quarks [4].

At the LHC neutral Higgs bosons are mainly produced via gluon-gluon fusion channel $gg \rightarrow \phi$ [5–14]. The weak boson fusion channel $qq \rightarrow qqV^*V^* \rightarrow qqh^0/qqH^0$ [15–17] as well as the associated production channel with weak bosons [18–20] also have significant contributions. Other production channels also have been studied, such as Higgs boson pair production [21–24] and associated production with top quark pair [25–28]. Nevertheless, the identification of the Higgs signature is difficult due to large QCD backgrounds against various Higgs particle decay modes. Recently, the Higgs boson and photon associated production channel has aroused interest [29]. For neutral Higgs boson and photon associated production, the otherwise dominating gluon fusion channel is forbidden via C-parity conservation, so quark-antiquark annihilation becomes dominant. In the case of CP-odd Higgs A^0 produced with a photon in a large $\tan\beta$ MSSM scenario, bottom quark annihilation $b\bar{b} \rightarrow A^0\gamma$ is of particular importance due to the large Yukawa coupling enhanced by the large $\tan\beta$. That compensates for the relatively small parton density of the bottom quark and the suppression from the QED vertex. Besides, associated production arising from weak boson fusion has also been studied in Ref. [30].

Since the bottom quark initial state contribution to $A^0\gamma$ associated production is sensitive to the bottom quark Yukawa coupling, the measurement of this channel at the LHC can

give detailed information of the Higgs coupling to the bottom quark. To provide a precise prediction of this associated production channel, we calculate the NLO QCD corrections to the total cross section and the kinematic distributions. In addition to effects from virtual or real gluons, loop effects from massive supersymmetry particles (the SUSY QCD effects), such as the sbottoms and the gluino, are also considered. Dimensional regularization scheme (DREG) (with naive γ_5 [31]) is adopted to regularize both ultraviolet (UV) and infrared (IR) divergences, which is equivalent to conventional supersymmetry-preserving dimensional reduction scheme (DRED) at the NLO level [32, 33]. For simplicity, we neglect the bottom quark mass except for in the Yukawa coupling. According to the simplified Aivazis-Collins-Olness-Tung scheme [34–36], such approximation is justified if the bottom quark appears as an initial parton.

The paper is organized as follows. In Sec. II, brief results for leading-order (LO) calculations are presented. In Sec. III, we present detailed calculations of NLO QCD corrections. In Sec. IV, we discuss a Monte Carlo simulation of the Higgs signature from the decay mode $A^0 \rightarrow \tau^+\tau^-$. In Sec. V, we provide numerical results for the total cross section and the differential cross sections with varying model parameters. Monte Carlo simulation results are also shown there.

II. LEADING-ORDER CROSS SECTION FOR NEUTRAL HIGGS AND PHOTON ASSOCIATED PRODUCTION

The LO cross section for $pp \rightarrow \gamma A^0$ in the MSSM has been studied in Ref. [29]. At tree level the only partonic subprocess is $b(p_1)\bar{b}(p_2) \rightarrow \gamma(p_3)A^0(p_4)$, and the corresponding two Feynman diagrams are shown in Fig. 1. The gluon-gluon fusion channel $gg \rightarrow \gamma A^0$ is forbidden by C-parity conservation [37–39]. In the tree level result we keep a finite bottom quark mass denoted as m_b . The cross section can be written as

$$d\hat{\sigma}^{LO} = \frac{1}{2\Phi} dPS^{(2)} |\overline{\mathcal{M}}|^2, \quad (1)$$

where $dPS^{(2)}$ is the 2-body final-state phase space and $1/2\Phi$ is the flux factor. The explicit expression for the differential cross section after averaging over spins and colors can be written as

$$\frac{d\hat{\sigma}}{d\hat{t}} = \frac{\alpha_{em} Q_b^2 \lambda_\phi^2}{4N_c(1-4r_b)} \left\{ \frac{F_1^\phi(\hat{s})}{(\hat{t} - m_b^2)(\hat{u} - m_b^2)} + F_2^\phi(\hat{s}) \left[\frac{1}{(\hat{t} - m_b^2)^2} + \frac{1}{(\hat{u} - m_b^2)^2} \right] \right\}, \quad (2)$$

with

$$F_1^\phi(\hat{s}) = (1 - r_\phi)^2 + 2r_\phi(1 - 2r_b), \quad F_2^\phi(\hat{s}) = -2r_b r_\phi, \quad (3)$$

where $Q_b = -1/3$ is the electric charge quantum number of the bottom quark, N_c the number of quark color, $r_b = m_b^2/\hat{s}$, $r_\phi = m_A^2/\hat{s}$, and $\lambda_\phi = -i\frac{m_b}{v}\tan\beta$ is the Yukawa coupling in MSSM which is proportional to the bottom quark mass. Here $v = 2m_W/g$ is the SM Higgs field VEV. In addition, the Mandelstam variables for $2 \rightarrow 2$ scattering process are introduced

$$\hat{s} = (p_1 + p_2)^2, \quad \hat{t} = (p_1 - p_3)^2, \quad \hat{u} = (p_1 - p_4)^2. \quad (4)$$

The hadronic cross section for $pp \rightarrow \gamma A^0$ at the LO is obtained straightforwardly by convoluting the parton level cross section with the parton distribution function (PDF),

$$\sigma^B = \int dx_1 dx_2 [G_{b/p}(x_1, \mu_F) G_{\bar{b}/p}(x_2, \mu_F) + (x_1 \leftrightarrow x_2)] \hat{\sigma}^B, \quad (5)$$

where μ_F is the factorization scale.

III. NLO QCD CALCULATIONS

The NLO QCD correction to γA^0 associated production consists of two parts. The virtual corrections account for virtual gluons as well as virtual supersymmetric particles such as the gluino \tilde{g} and the sbottoms $\tilde{b}_{1,2}$ in the loop diagrams. The real corrections result from the radiation of a real gluon or a massless bottom (anti-)quark. For the NLO calculations we follow the convention to work in $D = 4 - 2\epsilon$ dimensions and adopt the dimensional regularization approach (DREG) to regulate both the ultraviolet (UV) and the infrared (IR) divergences. As a good approximation, we take the bottom (anti-)quark mass to be zero except for in the Yukawa coupling.

A. Virtual corrections

The one-loop virtual corrections involve both the SM QCD contribution (8 diagrams as shown in Fig.2) and the SUSY QCD contribution (another 8 diagrams as shown in Fig.3). Either part is UV divergent. For the gluon loops we adopt \overline{MS} renormalization scheme to absorb those infinities, while for the SUSY particle loops we use the on-shell renormalization scheme instead.

The virtual correction is given by interfering the one-loop amplitude with the Born amplitude

$$d\hat{\sigma}^V = \frac{1}{2\hat{s}} dPS^{(2)} 2Re(\overline{\mathcal{M}^V} \cdot \mathcal{M}^B), \quad (6)$$

where $dPS^{(2)}$ is the 2-body final-state phase space and the flux factor is reduced to $1/2\hat{s}$ for massless (anti-)quark. In order to absorb all UV divergences, we introduce the renormalized bottom quark wavefunction for both the left-handed and the right-handed components $\psi_{bL,R}$ and the renormalized mass m_b , which are related to the bare mass m_{b0} and the bare wavefunction ψ_{b0} by

$$\begin{aligned} m_{b0} &= m_b + \delta m_b, \\ \psi_{b0} &= (1 + \delta Z_{bL})^{1/2} \psi_{bL} + (1 + \delta Z_{bR})^{1/2} \psi_{bR}, \end{aligned} \quad (7)$$

with $\psi_{bL,R} = (1 \mp \gamma_5)\psi_b/2$. By calculating the self-energy diagrams of the bottom quark propagator (shown in Fig.4), we obtain explicit expressions for the counter-terms which are in accordance with the results in Ref. [40, 41],

$$\begin{aligned} \left(\frac{\delta m_b}{m_b}\right)_{SM} &= -\frac{\alpha_s}{4\pi} C_F C(\epsilon) \frac{3}{\epsilon_{UV}}, \\ (\delta Z_{bL})_{SM} &= (\delta Z_{bR})_{SM} = \frac{\alpha_s}{4\pi} C_F C(\epsilon) \left\{ -\frac{3}{\epsilon_{UV}} + \frac{3}{\epsilon_{IR}} \right\}, \\ \left(\frac{\delta m_b}{m_b}\right)_{SUSY} &= -\frac{\alpha_s}{4\pi} C_F \sum_{i=1,2} \left\{ B_1(0, m_{\tilde{g}}^2, m_{\tilde{b}_i}^2) - \frac{m_{\tilde{g}}}{m_b} \sin 2\theta_{\tilde{b}} (-1)^i B_0(0, m_{\tilde{g}}^2, m_{\tilde{b}_i}^2) \right\}, \\ (\delta Z_{bL})_{SUSY} &= \frac{\alpha_s}{2\pi} C_F \sum_{i=1,2} (R_{i1}^{\tilde{b}})^2 B_1(0, m_{\tilde{g}}^2, m_{\tilde{b}_i}^2), \\ (\delta Z_{bR})_{SUSY} &= \frac{\alpha_s}{2\pi} C_F \sum_{i=1,2} (R_{i2}^{\tilde{b}})^2 B_1(0, m_{\tilde{g}}^2, m_{\tilde{b}_i}^2), \end{aligned} \quad (8)$$

where $C_F = 4/3$, $C(\epsilon) = \frac{\Gamma(1-\epsilon)}{\Gamma(1-2\epsilon)} \left(\frac{4\pi\mu_R^2}{\hat{s}}\right)^\epsilon$ and $B_{0,1}$ are the two-point integrals [42], as listed explicitly below

$$\begin{aligned} B_0(0, m_1^2, m_2^2) &= C(\epsilon) \left\{ \frac{1}{\epsilon_{UV}} - \frac{m_1^2 \ln \frac{m_1^2}{\hat{s}} - m_2^2 \ln \frac{m_2^2}{\hat{s}}}{m_1^2 - m_2^2} + 1 \right\}, \\ B_1(0, m_1^2, m_2^2) &= C(\epsilon) \left\{ -\frac{1}{2\epsilon_{UV}} + \frac{2m_1^4 \ln \frac{m_1^2}{\hat{s}} - 3m_1^4 + 4m_1^2 m_2^2 - m_2^4 + 2m_2^2(m_2^2 - 2m_1^2) \ln \frac{m_2^2}{\hat{s}}}{4(m_1^2 - m_2^2)^2} \right\}, \end{aligned} \quad (9)$$

where $m_{\tilde{b}_{1,2}}$ are the sbottom masses, $m_{\tilde{g}}$ is the gluino mass, and $R^{\tilde{b}}$ is a 2×2 rotation matrix

which transforms the gauge eigenstates into the mass eigenstates,

$$\begin{pmatrix} \tilde{b}_1 \\ \tilde{b}_2 \end{pmatrix} = R^{\tilde{b}} \begin{pmatrix} \tilde{b}_L \\ \tilde{b}_R \end{pmatrix}, \quad R^{\tilde{b}} = \begin{pmatrix} \cos \theta_{\tilde{b}} & \sin \theta_{\tilde{b}} \\ -\sin \theta_{\tilde{b}} & \cos \theta_{\tilde{b}} \end{pmatrix}, \quad (10)$$

with $0 \leq \theta_{\tilde{b}} \leq \pi$ by convention. Furthermore, the sbottom mass eigenvalues are solved by diagonalizing $M_{\tilde{b}}^2$,

$$\begin{pmatrix} m_{\tilde{b}_1}^2 & 0 \\ 0 & m_{\tilde{b}_2}^2 \end{pmatrix} = R^{\tilde{b}} M_{\tilde{b}}^2 (R^{\tilde{b}})^\dagger, \quad M_{\tilde{b}}^2 = \begin{pmatrix} m_{\tilde{b}_L}^2 & a_b m_b \\ a_b m_b & m_{\tilde{b}_R}^2 \end{pmatrix}, \quad (11)$$

with

$$\begin{aligned} m_{\tilde{b}_L}^2 &= M_{\tilde{Q}}^2 + m_b^2 + m_Z^2 \cos 2\beta C_{bL}, \\ m_{\tilde{b}_R}^2 &= M_{\tilde{D}}^2 + m_b^2 - m_Z^2 \cos 2\beta C_{bR}, \\ a_b &= A_b - \mu \tan \beta. \end{aligned} \quad (12)$$

Here $C_{bL} = -1/2 + \sin^2 \theta_W/3$, $C_{bR} = \sin^2 \theta_W/3$, and $M_{\tilde{b}}^2$ is the sbottom mass matrix. $M_{\tilde{Q},\tilde{D}}^2$ and A_b are soft SUSY-breaking parameters, and μ is the Higgsino mass parameter. Since the Yukawa coupling is proportional to the bottom quark mass, the renormalized vertex is obtained by expressing the bare mass m_{b0} in terms of the renormalized mass m_b plus a counter term δm_b ,

$$-i \frac{m_{b0}}{v} \tan \beta = -i \left[1 + \left(\frac{\delta m_b}{m_b} \right)_{SM} + \left(\frac{\delta m_b}{m_b} \right)_{SUSY} \right] \frac{m_b}{v} \tan \beta. \quad (13)$$

All the counter-term diagrams are shown in Fig.5.

With the one-loop counter-terms we write the renormalized virtual amplitude as

$$\mathcal{M}^V = \mathcal{M}_{SM}^{unren} + \mathcal{M}_{SUSY}^{unren} + \mathcal{M}^{con}. \quad (14)$$

The details of the calculation include the traditional Passarino-Veltman reduction procedure, in which Feynman amplitudes are reduced to master scalar integrals [43]. Here we list the analytic results for all the divergent scalar integrals (only the real part is kept) involved in

the calculation,

$$\begin{aligned}
B_0(\hat{t}, 0, 0) &= C(\epsilon) \left[\frac{1}{\epsilon_{UV}} + 2 - \ln \left(\frac{-\hat{t}}{\hat{s}} \right) \right], \\
B_0(\hat{u}, 0, 0) &= C(\epsilon) \left[\frac{1}{\epsilon_{UV}} + 2 - \ln \left(\frac{-\hat{u}}{\hat{s}} \right) \right], \\
B_0(m_A^2, 0, 0) &= C(\epsilon) \left[\frac{1}{\epsilon_{UV}} + 2 - \ln r_\phi \right], \\
C_0(0, 0, \hat{t}, 0, 0, 0) &= C(\epsilon) \left(\frac{1}{-\hat{t}} \right) \left[-\frac{1}{\epsilon_{IR}^2} + \frac{\ln(-\hat{t}/\hat{s})}{\epsilon_{IR}} - \frac{1}{2} \ln^2 \left(\frac{-\hat{t}}{\hat{s}} \right) - \frac{\pi^2}{6} \right], \\
C_0(0, 0, \hat{u}, 0, 0, 0) &= C(\epsilon) \left(\frac{1}{-\hat{u}} \right) \left[-\frac{1}{\epsilon_{IR}^2} + \frac{\ln(-\hat{u}/\hat{s})}{\epsilon_{IR}} - \frac{1}{2} \ln^2 \left(\frac{-\hat{u}}{\hat{s}} \right) - \frac{\pi^2}{6} \right], \\
C_0(0, m_A^2, \hat{s}, 0, 0, 0) &= C(\epsilon) \left(\frac{1}{1-r_\phi} \right) \left[\frac{\ln r_\phi}{\epsilon_{IR}} - \frac{\ln^2 r_\phi}{2} \right], \\
C_0(0, m_A^2, \hat{t}, 0, 0, 0) &= C(\epsilon) \left(\frac{1}{m_A^2 - \hat{t}} \right) \left[\frac{1}{\epsilon_{IR}} \ln \left(\frac{-\hat{t}}{m_A^2} \right) - \frac{1}{2} \ln r_\phi \ln \left(\frac{-\hat{t}}{m_A^2} \right) \right. \\
&\quad \left. - \frac{1}{2} \ln \left(\frac{-\hat{t}}{\hat{s}} \right) \ln \left(\frac{-\hat{t}}{m_A^2} \right) - \frac{\pi^2}{2} \right], \\
C_0(0, m_A^2, \hat{u}, 0, 0, 0) &= C(\epsilon) \left(\frac{1}{m_A^2 - \hat{u}} \right) \left[\frac{1}{\epsilon_{IR}} \ln \left(\frac{-\hat{u}}{m_A^2} \right) - \frac{1}{2} \ln r_\phi \ln \left(\frac{-\hat{u}}{m_A^2} \right) \right. \\
&\quad \left. - \frac{1}{2} \ln \left(\frac{-\hat{u}}{\hat{s}} \right) \ln \left(\frac{-\hat{u}}{m_A^2} \right) - \frac{\pi^2}{2} \right], \\
D_0(0, m_A^2, 0, 0, \hat{t}, \hat{s}, 0, 0, 0, 0) &= C(\epsilon) \left(\frac{1}{-\hat{t}} \right) \left[-\frac{2}{\epsilon_{IR}^2} + \frac{2}{\epsilon_{IR}} \ln \left(\frac{-\hat{t}}{m_A^2} \right) + \ln r_\phi^2 \right. \\
&\quad \left. + 2 \left(\text{Li}_2 \left(\frac{\hat{s} - m_A^2}{\hat{s}} \right) - \text{Li}_2 \left(\frac{\hat{s} - m_A^2}{\hat{t}} \right) \right) - \pi^2 \right], \\
D_0(0, m_A^2, 0, 0, \hat{u}, \hat{s}, 0, 0, 0, 0) &= C(\epsilon) \left(\frac{1}{-\hat{u}} \right) \left[-\frac{2}{\epsilon_{IR}^2} + \frac{2}{\epsilon_{IR}} \ln \left(\frac{-\hat{u}}{m_A^2} \right) + \ln r_\phi^2 \right. \\
&\quad \left. + 2 \left(\text{Li}_2 \left(\frac{\hat{s} - m_A^2}{\hat{s}} \right) - \text{Li}_2 \left(\frac{\hat{s} - m_A^2}{\hat{u}} \right) \right) - \pi^2 \right],
\end{aligned} \tag{15}$$

We then find that the renormalized amplitude \mathcal{M}^V is UV finite, but still contains IR poles, which is given by

$$\mathcal{M}^V = \frac{\alpha_s}{2\pi} C(\epsilon) \left\{ \frac{A_2^V}{\epsilon_{IR}^2} + \frac{A_1^V}{\epsilon_{IR}} \right\} \mathcal{M}^B, \tag{16}$$

with

$$A_2^V = -C_F, \quad A_1^V = -\frac{3}{2}C_F, \tag{17}$$

which demonstrates that the IR divergent part is factorized and consists of both soft and collinear singularities. The former is canceled when we combine the virtual corrections with the real corrections, while the latter can be canceled by adopting the mass factorization procedure.

B. Real gluon emission

The Feynman diagrams for the radiation of a real gluon $b(p_1)\bar{b}(p_2) \rightarrow \gamma(p_3)A^0(p_4)g(p_5)$ are shown in Fig.6. The partonic cross section can be written as

$$d\hat{\sigma}^R = \frac{1}{2\hat{s}} dPS^{(3)} |\overline{\mathcal{M}^B}|^2, \quad (18)$$

The 3-body phase space integration for real gluon emission contains soft and collinear singularities. We adopt the two cutoff phase space slicing method [44] to isolate all the IR singularities, which introduces two small cutoffs δ_s and δ_c to divide the phase space into three parts.

First, the soft cutoff δ_s separates the phase space into the soft region $E_5 \leq \delta_s \sqrt{\hat{s}}/2$ and the hard region otherwise in the partonic center of mass (CM) frame. Thus the partonic cross section can be written as a sum of the contributions from both regions,

$$\hat{\sigma}^R = \hat{\sigma}^S + \hat{\sigma}^H. \quad (19)$$

Furthermore, the hard piece can be divided into two sub-regions by introducing a collinear cutoff δ_c . Within the hard collinear region $(p_1 + p_5)^2 \leq \delta_c \hat{s}$ or $(p_2 + p_5)^2 \leq \delta_c \hat{s}$ all the collinear divergences are isolated, leaving the hard non-collinear region free of any IR singularities. Similarly we have for the partonic cross section

$$\hat{\sigma}^H = \hat{\sigma}^{HC} + \hat{\sigma}^{\overline{HC}}. \quad (20)$$

Below we proceed to discuss the details of calculation in each region of the phase space.

1. Hard non-collinear region

For the hard non-collinear region where no IR singularity is present, the phase space integration can be calculated numerically. For the 3-body phase space a convenient parameterization with 4 non-trivial parameters is given below,

$$dPS^{(3)} = \frac{\hat{s}}{32(2\pi)^4} dX_1 dX_2 d\cos\theta d\varphi. \quad (21)$$

Here $-1 \leq \cos\theta \leq 1$ and $0 \leq \varphi \leq 2\pi$ represent the solid angle in the CM frame into which the final-state photon is scattered. Besides, $X_{1,2}$ are dimensionless variables which

determine the final state energy in the partonic CM frame through

$$E_3 = \frac{\sqrt{\hat{s}}}{2}(1 - X_2), \quad E_4 = \frac{\sqrt{\hat{s}}}{2}(X_1 + X_2), \quad E_5 = \frac{\sqrt{\hat{s}}}{2}(1 - X_1). \quad (22)$$

The integration region for them is inside the unit square in the parameter plane and are subject to kinematic constraints $X_1 + X_2 \leq 1 + r_\phi$ and $X_1 X_2 \geq r_\phi$.

2. Soft region

In the limit of vanishing gluon energy (the eikonal approximation), the squared matrix element for real gluon emission can be factorized into the Born piece multiplied by an eikonal factor Φ_{eik}

$$\overline{|\mathcal{M}^R(b\bar{b} \rightarrow \gamma A^0 + g)|^2} \xrightarrow{soft} (4\pi\alpha_s\mu_R^{2\epsilon}) \overline{|\mathcal{M}^B|^2} \Phi_{eik}, \quad (23)$$

where the eikonal factor can be written explicitly

$$\Phi_{eik} = C_F \left\{ \frac{-p_1^2}{(p_1 \cdot p_5)^2} + \frac{-p_2^2}{(p_2 \cdot p_5)^2} + \frac{2(p_1 \cdot p_2)}{(p_1 \cdot p_5)(p_2 \cdot p_5)} \right\} = C_F \frac{\hat{s}}{(p_1 \cdot p_5)(p_2 \cdot p_5)}. \quad (24)$$

Meanwhile the 3-body phase space is factorized into the following form

$$dPS^{(3)}(b\bar{b} \rightarrow \gamma A^0 + g) \xrightarrow{soft} dPS^{(2)}(b\bar{b} \rightarrow \gamma A^0) dS, \quad (25)$$

with dS the soft gluon phase space to be integrated

$$dS = \frac{1}{\pi} \left(\frac{4}{\hat{s}} \right)^{-\epsilon} \int_0^{\delta_s \sqrt{\hat{s}}/2} dE_5 E_5^{1-2\epsilon} \int_0^\pi \sin^{1-2\epsilon} \varphi_1 d\varphi_1 \int_0^\pi \sin^{-2\epsilon} \varphi_2 d\varphi_2. \quad (26)$$

After performing the integrations we arrive at a form where IR singularities are explicit

$$d\hat{\sigma}^S = d\hat{\sigma}^B \frac{\alpha_s}{2\pi} C(\epsilon) \left(\frac{A_2^S}{\epsilon^2} + \frac{A_1^S}{\epsilon} + A_0^S \right), \quad (27)$$

with

$$A_2^S = 2C_F, \quad A_1^S = -4C_F \ln \delta_s, \quad A_0^S = 4C_F \ln^2 \delta_s. \quad (28)$$

3. Hard collinear region

In the hard collinear region, the factorization theorem [45, 46] states that the squared amplitude can be factorized into the squared Born amplitude multiplied by the unregulated

Altarelli-Parisi splitting function as long as the matrix element is calculated under the collinear limit of kinematic configuration.

$$\overline{|\mathcal{M}^R(b\bar{b} \rightarrow \gamma A^0 + g)|^2} \xrightarrow{coll.} (4\pi\alpha_s\mu_R^{2\epsilon}) \overline{|\mathcal{M}^B(b'\bar{b} \rightarrow \gamma A^0; \hat{s}' = z\hat{s})|^2} \frac{-2P_{b'b}(z, \epsilon)}{z(p_1 - p_5)^2}. \quad (29)$$

Moreover, the phase space can also be factorized in the collinear limit,

$$dPS^{(3)}(b\bar{b} \rightarrow \gamma A^0 + g) \xrightarrow{coll.} dPS^{(2)}(b'\bar{b} \rightarrow \gamma A^0) \frac{(4\pi)^\epsilon}{16\pi^2\Gamma(1-\epsilon)} dz dt_{15} [-(1-z)t_{15}]^{-\epsilon}, \quad (30)$$

with $t_{15} = (p_1 - p_5)^2$. After convoluting with the PDFs we obtain an expression for the inclusive cross section where collinear singularities are explicit in terms of $1/\epsilon$ poles [44]

$$\begin{aligned} d\sigma_{b\text{-splitting}}^{HC} = d\hat{\sigma}^B(b\bar{b} \rightarrow \gamma A^0) & \left[G_{b/p}\left(\frac{x_1}{z}\right) G_{\bar{b}/p}(x_2) + (x_1 \leftrightarrow x_2) \right] \\ & \times \frac{\alpha_s}{2\pi} C(\epsilon) \left(\frac{1}{-\epsilon} \right) \delta_c^{-\epsilon} P_{bb}(z, \epsilon) \frac{dz}{z} \left(\frac{1-z}{z} \right)^{-\epsilon} dx_1 dx_2. \end{aligned} \quad (31)$$

A similar term which gives exactly the same contribution is also present to account for initial-state anti-quark splitting. So the complete collinear piece is

$$\begin{aligned} d\sigma^{HC} = & \left[G_{b/p}\left(\frac{x_1}{z}\right) G_{\bar{b}/p}(x_2) + G_{\bar{b}/p}\left(\frac{x_1}{z}\right) G_{b/p}(x_2) + (x_1 \leftrightarrow x_2) \right] d\hat{\sigma}^B(b\bar{b} \rightarrow \gamma A^0) \\ & \times \frac{\alpha_s}{2\pi} C(\epsilon) \left(\frac{1}{-\epsilon} \right) \delta_c^{-\epsilon} P_{bb}(z, \epsilon) \frac{dz}{z} \left(\frac{1-z}{z} \right)^{-\epsilon} dx_1 dx_2, \end{aligned} \quad (32)$$

where the unregulated Altarelli-Parisi splitting functions are written explicitly as

$$P_{bb}(z, \epsilon) = P_{\bar{b}\bar{b}}(z, \epsilon) = C_F \left(\frac{1+z^2}{1-z} - \epsilon(1-z) \right). \quad (33)$$

where $G_{b(\bar{b})/p}(x)$ is temporarily the bare PDF. Due to the non-soft constraint we have $x_1 \leq z \leq 1 - \delta_s$.

C. Massless bottom (anti-)quark emission

At $\mathcal{O}(\alpha_s)$ of the perturbative expansion bg (or $\bar{b}g$) initial subprocesses should be taken into consideration, with the relevant Feynman diagrams shown in Fig.7.

The treatment is much the same as to $b\bar{b}$ annihilation except for some differences. First, the radiation of a massless (anti-)quark contains no soft divergence. Hence there is no need to introduce a soft cutoff, and the 3-body phase space is divided into a collinear region and a non-collinear region, for the latter numerical calculation is straightforward.

There is also collinear singularity arising from collinear emission of massless (anti-)quark. The factorization treatment in the previous subsection applies if we introduce the collinear cutoff δ_c to separate the collinear region and isolate the collinear poles. Combining the non-collinear piece and collinear piece we obtain the cross section

$$d\sigma^{add.} = \sum_{\alpha=b,\bar{b}} d\hat{\sigma}^{\overline{C}}(g\alpha \rightarrow \gamma A^0 + \alpha) [G_{g/p}(x_1)G_{\alpha/p}(x_2) + (x_1 \leftrightarrow x_2)] dx_1 dx_2 \\ + d\hat{\sigma}^B(b\bar{b} \rightarrow \gamma A^0) \frac{\alpha_s}{2\pi} C(\epsilon) \left(-\frac{1}{\epsilon}\right) \delta_c^{-\epsilon} \left[P_{bg}(z, \epsilon) G_{g/p}\left(\frac{x_1}{z}\right) G_{\bar{b}/p}(x_2) + P_{\bar{b}g}(z, \epsilon) G_{g/p}\left(\frac{x_1}{z}\right) G_{b/p}(x_2) \right. \\ \left. + (x_1 \leftrightarrow x_2) \right] \times \frac{dz}{z} \left(\frac{1-z}{z}\right)^{-\epsilon} dx_1 dx_2, \quad (34)$$

where the unregulated Altarelli-Parisi splitting functions are written explicitly as

$$P_{bg}(z, \epsilon) = P_{\bar{b}g}(z, \epsilon) = \frac{3}{8} C_F (z^2 + (1-z)^2 - 2z(1-z)\epsilon). \quad (35)$$

Further collinear singularity can still arise in the configuration in which the photon is emitted in parallel with the additional final-state quark. By comparison, such singularity does not exist for a final-state gluon at next-to-leading order. A criterion for isolated photon has been suggested in Refs. [47], which defines an IR-safe cross section decoupled with hadronic fragmentation and at the same time allows for complete cancelation of soft gluon divergence. For the case of only one final-state parton such criterion is equivalent to the kinematic cut

$$p_T^j < \frac{1 - \cos \Delta R_{j\gamma}}{1 - \cos \Delta R_0} p_T^\gamma, \quad \text{for } \Delta R_{j\gamma} < \Delta R_0, \quad (36)$$

where j stands for either the final-state (anti-)quark or the final-state gluon, and $\Delta R_{j\gamma}$ is the cone distance in the rapidity-azimuthal angle plane between the parton and the photon. Throughout our calculation we choose the cone-size parameter $\Delta R_0 = 0.4$.

D. Mass factorization

Since the real correction and the virtual correction combined are incomplete to cancel all the divergences, the procedure of mass factorization is necessary. Generally, the scale-dependent PDF $G_{\alpha/\beta}(x, \mu_F)$ under \overline{MS} scheme can be written following Ref. [44]

$$G_{\alpha/p}(x, \mu_F) = G_{\alpha/p}(x) + \sum_{\beta} \left(-\frac{1}{\epsilon}\right) \frac{\alpha_s}{2\pi} C(\epsilon) \left(\frac{\mu_F^2}{\hat{s}}\right)^\epsilon \int_x^1 \frac{dz}{z} P_{\alpha\beta}(z) G_{\beta/p}\left(\frac{x}{z}\right). \quad (37)$$

The Altarelli-Parisi splitting function in the above formula is independent of ϵ which is defined by

$$P_{\alpha\beta}(y, \epsilon) = P_{\alpha\beta}(y) + \epsilon P'_{\alpha\beta}(y). \quad (38)$$

Thus a collinear counter-term of $\mathcal{O}(\alpha_s)$ is obtained from the LO piece and will be used to cancel the collinear divergence. If we combine the counter-term with the hard collinear pieces, from both $b\bar{b}$ channel and bg (or $\bar{b}g$) channel, we will find the remaining collinear piece in the following form,

$$\begin{aligned} d\sigma^C = & d\hat{\sigma}^B \frac{\alpha_s}{2\pi} C(\epsilon) \left\{ \tilde{G}_{b/p}(x_1, \mu_F) G_{\bar{b}/p}(x_2, \mu_F) + G_{b/p}(x_1, \mu_F) \tilde{G}_{\bar{b}/p}(x_2, \mu_F) \right. \\ & \left. + \sum_{\alpha=b, \bar{b}} \left[\frac{A_1^{SC}(\alpha \rightarrow \alpha g)}{\epsilon} + A_0^{SC}(\alpha \rightarrow \alpha g) \right] G_{b/p}(x_1, \mu_F) G_{\bar{b}/p}(x_2, \mu_F) + (x_1 \leftrightarrow x_2) \right\} dx_1 dx_2. \end{aligned} \quad (39)$$

The summed terms with $A_{1,0}^{SC}$ are a result of an overlap of both soft and collinear phase space regions. One can explicitly write

$$\begin{aligned} A_1^{SC}(b \rightarrow bg) &= A_1^{SC}(\bar{b} \rightarrow \bar{b}g) = C_F \left(2 \ln \delta_s + \frac{3}{2} \right), \\ A_0^{SC}(b \rightarrow bg) &= A_0^{SC}(\bar{b} \rightarrow \bar{b}g) = C_F \left(2 \ln \delta_s + \frac{3}{2} \right) \ln \frac{\hat{s}}{\mu_F^2}, \end{aligned} \quad (40)$$

and the tilded G functions

$$\tilde{G}_{\alpha/p}(x, \mu_F) = \sum_{\beta} \int_x^{1-\delta_s \delta_{\alpha\beta}} \frac{dy}{y} \tilde{P}_{\alpha\beta}(y) G_{\beta/p}\left(\frac{x}{y}, \mu_F\right), \quad (41)$$

with

$$\tilde{P}_{\alpha\beta}(y) = P_{\alpha\beta}(y) \ln \left(\delta_c \frac{1-y}{y} \frac{\hat{s}}{\mu_F^2} \right) - P'_{\alpha\beta}(y). \quad (42)$$

Now we can confirm that all the divergences have been canceled, since

$$\begin{aligned} 2A_2^V + A_2^S &= 0, \\ 2A_1^V + A_1^S + \sum_{\alpha=b, \bar{b}} A_1^{SC}(\alpha \rightarrow \alpha g) &= 0. \end{aligned} \quad (43)$$

Putting together all pieces, we find a finite result of the NLO QCD total cross section for $pp \rightarrow \gamma A^0 + X$

$$\begin{aligned} \sigma^{NLO} = & \int \left\{ dx_1 dx_2 \left[G_{b/p}(x_1, \mu_F) G_{\bar{b}/p}(x_2, \mu_F) + (x_1 \leftrightarrow x_2) \right] (\hat{\sigma}^B + \hat{\sigma}^V + \hat{\sigma}^S + \hat{\sigma}^{\overline{HC}}) + \hat{\sigma}^C \right\} \\ & + \sum_{\alpha=b, \bar{b}} \int dx_1 dx_2 \left[G_{\alpha/p}(x_1, \mu_F) G_{g/p}(x_2, \mu_F) + (x_1 \leftrightarrow x_2) \right] \hat{\sigma}^{\overline{C}}(\alpha g \rightarrow \gamma A^0 + \alpha). \end{aligned} \quad (44)$$

Kinematic cuts
$p_T^\gamma > 30 \text{ GeV}, p_T^\tau > 20 \text{ GeV}$
$ \eta^{\gamma,\tau} < 2.5$
$\Delta R_{\gamma\tau} > 0.7, \Delta R_{\tau\tau} > 0.7$
$0.9m_A < M_{\tau\tau} < 1.1m_A$
$\Delta\phi_{\tau\tau} < 2.9$

TABLE I: Kinematic cuts imposed in the Monte Carlo simulation

We see that the total cross section depends on two undetermined scales: the renormalization scale μ_R and the factorization scale μ_F .

IV. MONTE CARLO SIMULATION

At the LHC, the leptonic decay mode $A^0 \rightarrow \tau^+\tau^-$ will be the most promising signature in the search of A^0 . For a moderate Higgs mass, the branch ratio $\Gamma_{A^0 \rightarrow \tau^+\tau^-}$ is around 10%, but the QCD background is much smaller compared with that in the decay mode $A^0 \rightarrow b\bar{b}$. Therefore we also conduct a Monte Carlo simulation study of the $\tau^+\tau^- + \gamma$ signature against the dominant irreducible SM background, namely the off-shell production of gauge bosons $q\bar{q} \rightarrow \gamma Z^*/\gamma\gamma^* \rightarrow \gamma\tau^+\tau^-$. For the calculation of the background we use the package CompHep v4.5.1 [48].

We impose the transverse momentum cuts $p_T^\gamma > 30 \text{ GeV}$, $p_T^\tau > 20 \text{ GeV}$, and the pseudo-rapidity cuts $|\eta^{\gamma,\tau}| < 2.5$ for the photon and the tau leptons. We require the distance $\Delta R_{\gamma\tau} > 0.7$, $\Delta R_{\tau\tau} > 0.7$ to ensure well-separated final states. To reconstruct the on-shell Higgs boson A^0 , we also demand that the tau pair invariant mass is within the window $[0.9m_A, 1.1m_A]$. Besides, an additional cut on the azimuthal angles $\Delta\phi_{\tau\tau} < 2.9$ is also imposed on the tau lepton pair, which is very effective at suppressing the false signature arising from a high- p_T photon radiated from one of the tau leptons. After all the above kinematic cuts are applied, the SM background cross section can be reduced by 3 orders of magnitude. All these cuts, summarized in Tab. I, are in accord with Ref. [29] in order to compare our results with theirs.

V. NUMERICAL RESULTS

This section is arranged as follows. First, we present the numerical results for the complete NLO QCD corrected cross sections to $A^0\gamma$ associated production. Then we present simulation results of the $\tau^+\tau^- + \gamma$ signature under various kinematic cuts, for both the integrated cross section and differential cross sections. It is worth to mention that in our results $H^0 - A^0$ degeneracy is not assumed. For large m_A and large $\tan\beta$, such degeneracy doubles the cross section.

A. NLO total cross section calculations

In this section, we present the results of the inclusive total cross section for $pp \rightarrow \gamma A^0 + X$ at the LHC with total colliding energy $\sqrt{s} = 14$ TeV. Throughout our calculations CTEQ6L1 parton structure functions are used for LO cross sections and CTEQ6M used for the NLO ones. We impose the photon transverse momentum cut $p_T^\gamma > 30$ GeV and pseudo-rapidity cut $|\eta^\gamma| < 2.5$. We choose the following SM input parameters [49]

$$\begin{aligned} m_t = 172.4 \text{ GeV}, \quad G_F = 1.16637 \times 10^{-5} \text{ GeV}^{-2}, \quad m_W = 80.398 \text{ GeV}, \quad m_Z = 91.1876 \text{ GeV}, \\ \alpha_s(m_Z) = 0.1176, \quad m_b^{\text{pole}} = 4.68 \text{ GeV}, \quad m_b(m_b^{\text{pole}}) = 4.20 \text{ GeV}, \quad \alpha_{em}(m_W) = 1/128. \end{aligned} \quad (45)$$

Both the strong coupling α_s and the running bottom quark mass [50] are evolved up to two loops in QCD

$$m_b(\mu_R) = U_6(\mu_R, m_t) U_5(m_t, m_b^{\text{pole}}) m_b(m_b^{\text{pole}}), \quad (46)$$

where the evolution factor U_f is given by

$$U_f(\mu_2, \mu_1) = \left(\frac{\alpha_s(\mu_2)}{\alpha_s(\mu_1)} \right)^{d^{(f)}} \left[1 + \frac{\alpha_s(\mu_1) - \alpha_s(\mu_2)}{4\pi} J^{(f)} \right], \quad (47)$$

$$d^{(f)} = \frac{12}{33 - 2f}, \quad J^{(f)} = -\frac{8982 - 504f + 40f^2}{3(33 - 2f)^2}, \quad (48)$$

and f denotes the number of active quark flavors.

In the large $\tan\beta$ scenario, perturbative calculation is improved by resumming the $\tan\beta$ -enhanced threshold SUSY QCD corrections [50]. It is equivalent to make the following

replacement for the tree-level bottom quark running mass

$$m_b(\mu_R) \rightarrow \frac{m_b(\mu_R)}{1 + \Delta_b(\mu_{SUSY})}, \quad \Delta_b(\mu_{SUSY}) = \frac{\alpha_s(\mu_{SUSY})}{2\pi} C_F m_{\tilde{g}} \mu I(m_{\tilde{b}_1}, m_{\tilde{b}_2}, m_{\tilde{g}}) \tan \beta, \quad (49)$$

where the auxiliary function is defined by

$$I(a, b, c) = -\frac{1}{(a^2 - b^2)(b^2 - c^2)(c^2 - a^2)} \left(a^2 b^2 \ln \frac{a^2}{b^2} + b^2 c^2 \ln \frac{b^2}{c^2} + c^2 a^2 \ln \frac{c^2}{a^2} \right), \quad (50)$$

To avoid double-counting, an additional finite counter-term for the bottom quark mass should be introduced

$$\frac{\delta \tilde{m}_b}{m_b} = \Delta_b \left(1 + \frac{1}{\tan^2 \beta} \right). \quad (51)$$

For the SUSY QCD contribution the package SPheno v2.2.2 is used to calculate all the parameters in the MSSM [51]. We choose the minimal supergravity scenario (mSUGRA) in which various MSSM parameters are constrained by only five free input parameters at the grand unification scale: $m_{1/2}$, m_0 , A_0 , $\tan \beta$ and the sign of μ . The first three parameters $m_{1/2}$, m_0 , A_0 are, respectively, the universal gaugino mass, the universal scalar mass, and the trilinear soft breaking parameter of the superpotential [53]. We fix $m_{1/2} = 200$ GeV, $A_0 = 0$ while $\tan \beta$ and the sign of μ are left as free parameters. The desired value of m_A is obtained by tuning m_0 . Unless specified, the factorization scale μ_F and the renormalization scale μ_R are always set equal at $\mu_F = \mu_R = \mu_0 = m_A/2$. Besides, a third scale, the SUSY scale μ_{SUSY} which comes into effect by threshold SUSY QCD resummation to the bottom quark Yukawa coupling, is chosen to be $\mu_{SUSY} = 2$ TeV.

In Fig.8, the NLO total cross section is plotted against δ_s and δ_c over a wide range of variation at the SUSY benchmark point SPS 4 [52]. For the NLO corrections, the real/hard correction depends on δ_s and δ_c , the virtual and soft gluon pieces combined depends only on δ_s , and the hard collinear part depends only on δ_c . However, when all pieces are added together, the dependence on δ_s and δ_c is canceled out as long as sufficiently small values of δ_s and δ_c are chosen. From Fig. 9, in which the SPS 4 benchmark point is also chosen, we can see that the complete NLO QCD corrections improve the scale dependence as compared to the LO results for $m_A/4 < \mu_0 < m_A$. In addition, the SUSY QCD correction is found to further reduce the scale uncertainty even though it is much smaller than the SM QCD correction.

In Fig.10 and Fig.11, we plot the total cross sections with scale uncertainties for the inclusive $pp \rightarrow \gamma A^0 + X$ production as functions of the Higgs boson mass m_A . A positive

MSSM soft breaking parameter μ , which is favored by the measurement of $(g-2)_\mu$ [54], is of particular interest. However, in the $\mu > 0$ scenario the mass of A^0 can not be smaller than 200 GeV. Assuming $\tan\beta = 50$, the total cross section decreases rapidly as the Higgs boson becomes heavier, from $60 \sim 70$ fb for relatively light Higgs boson mass $m_A = 300$ GeV to a mere 15 fb for much heavier Higgs boson mass $m_A = 500$ GeV. For the case of $\tan\beta = 10$ the total cross section is an order smaller. The NLO corrections efficiently reduce the total scale dependence of the cross sections in the light Higgs boson mass region but not the heavy mass region. This is because that the factorization and renormalization scale dependence cancels exactly in the heavy mass region at the LO. And we have checked that the factorization and renormalization scale dependence is indeed improved separately. Also in Fig.12 and Fig.13, K-factor as a function of the Higgs boson mass m_A is plotted to show how much the NLO QCD corrections can modify the LO prediction. Taking the case of $\tan\beta = 50$ for example, QCD corrections from the pure SM contributions typically increase the total cross section by around $22 \sim 16\%$ for $300 \text{ GeV} \leq m_A \leq 500 \text{ GeV}$. The SUSY QCD corrections can suppress the cross section by as much as 12% for light Higgs mass $m_A = 200$ GeV. Nevertheless, the suppression drops to less than 2% in magnitude for heavy Higgs mass $m_A = 500$ GeV. The scale uncertainties of the NLO total cross sections range from 10% to 20% of the LO total cross sections with the varying of m_A and $\tan\beta$ as can be seen from Fig.12 and Fig.13.

B. Simulation results

In Tab.II, we present the results of the integrated signal cross section including the LO results, the NLO results without the SUSY QCD corrections, and the complete NLO results. For the mSUGRA input parameters, we fix $m_{1/2} = 200$ GeV, $A_0 = 0$, $\tan\beta = 50$ and $\mu > 0$, and tune m_0 to obtain Higgs mass $m_A = 200$ GeV, 300 GeV, 500 GeV. For the heavier Higgs mass cases, we choose transverse momentum cut, $p_T^\gamma > 40$ GeV, 50 GeV for $m_A = 300$ GeV, 500 GeV, respectively. Other cuts are the same as what has been mentioned in Sec. IV. Moreover, an integrated luminosity of 100 fb^{-1} and a τ -pair detection efficiency $\epsilon_{\tau\tau} = 0.2$ are assumed to evaluate the signal significance $\mathcal{S} = N(S)/\sqrt{N(B)}$.

For the case of $m_A = 200$ GeV in which a relatively large signal cross section and a high significance can be obtained, we investigate the NLO QCD effects more closely by studying various differential cross sections. Fig.14 shows the invariant mass distribution $d\sigma/dM_{\tau\tau}$ of

m_A [GeV]	Background	LO		NLO (no SUSY)		NLO	
	σ_B [fb]	σ_S [fb]	\mathcal{S}	σ_S [fb]	\mathcal{S}	σ_S [fb]	\mathcal{S}
200	3.44	8.38	20.2	10.8	26.0	9.84	23.7
300	1.12	1.91	8.05	2.39	10.0	2.30	9.71
500	0.270	0.287	2.47	0.354	3.05	0.349	3.00

TABLE II: Signal cross section σ_S , background cross section σ_B and significance \mathcal{S} for the associated production $pp \rightarrow A^0\gamma \rightarrow \tau^+\tau^-\gamma$ at the LHC. We set the mSUGRA input parameters $m_{1/2} = 200$ GeV, $A_0 = 0$, $\tan\beta = 50$ and $\mu > 0$.

the tau lepton pair. With the central region significantly enhanced by the NLO corrections, the mass peak for A^0 is clearly seen above the background. Fig.15 shows the photon transverse momentum distribution $d\sigma/dp_T^\gamma$. The NLO QCD effects can enhance the LO results by as much as 13%, depending on the specific value of p_T^γ . Nevertheless, no significant distortion of the curve is found. In Fig.16, we present the photon pseudo-rapidity distribution $d\sigma/d\eta^\gamma$ together with the background. The NLO effects lead to moderate enhancement of the distribution, but do not change the shape of the curve either. Analysis of these differential cross sections shows that the NLO QCD corrections generally enhance the signature.

VI. CONCLUSIONS

In conclusion, we have investigated the complete NLO QCD corrections to the inclusive total cross sections of $A^0\gamma$ associated production at the LHC in the MSSM. Our results show that the NLO corrections can enhance the total cross sections by 25% \sim 15% for Higgs mass $200 \text{ GeV} < m_A < 500 \text{ GeV}$ and $\tan\beta = 50$. The SUSY QCD correction is negative and significant for light Higgs mass $m_A = 200 \text{ GeV}$, but is negligible for heavy Higgs mass $m_A = 500 \text{ GeV}$. The NLO corrections generally reduce the dependence of the total cross sections on the renormalization/factorization scale. Assuming a normal luminosity of 100 fb^{-1} , we simulated the $\tau^+\tau^- + \gamma$ signature including the complete NLO QCD effects at the LHC, and found an observable signature above the SM background with a high signal significance in some regions of the MSSM parameter space allowed by the current experiments. Thus it can be expected that the LHC has the potential to discover a CP-

odd Higgs boson with a mass of $200\text{ GeV} \sim 300\text{ GeV}$ via the photon associated production channel for large $\tan\beta$.

Acknowledgments

This work was supported in part by the National Natural Science Foundation of China, under Grants No. 10721063, No. 10975004 and No. 10635030.

-
- [1] F. Gianotti *et al.* Eur. Phys. J. **C 39**, 293 (2005).
 - [2] R. Barate *et al.* [LEP WG for Higgs boson searches], Phys. Lett. **B 565**, 61 (2003).
 - [3] S. P. Martin, *A Supersymmetry Primer*, arXiv:hep-ph/9709356v5.
 - [4] J. R. Ellis *et al.*, arXiv:0706.0977 [hep-ph].
 - [5] H. M. Georgi, S. L. Glashow, M. E. Machacek and D. V. Nanopoulos, Phys. Rev. Lett. **40**, 692 (1978).
 - [6] M. Spira, A. Djouadi, D. Graudenz and P. M. Zerwas, Phys. Lett. **B 318** (1993) 347; Nucl. Phys. **B 453**, 17 (1995).
 - [7] S. Dawson, A. Djouadi and M. Spira, Phys. Rev. Lett. **77**, 16 (1996).
 - [8] A. Djouadi and M. Spira, Phys. Rev. **D 62**, 014004 (2000).
 - [9] R. V. Harlander and W. B. Kilgore, Phys. Rev. Lett. **88**, 201801 (2002); JHEP 0210 017 (2002).
 - [10] C. Anastasiou and K. Melnikov, Nucl. Phys. **B 646**, 220 (2002); Phys. Rev. **D 67**, 037501 (2003).
 - [11] V. Ravindran, J. Smith and W. L. van Neerven, Nucl. Phys. **B 665**, 325 (2003).
 - [12] S. Catani, D. de Florian, M. Grazzini and P. Nason, JHEP 0307, 028 (2003).
 - [13] R. V. Harlander and M. Steinhauser, Phys. Lett. **B 574**, 258 (2003); Phys. Rev. **D 68**, 111701 (2003); JHEP 0409 066 (2004).
 - [14] A. Kulesza, G. Sterman and W. Vogelsang, Phys. Rev. **D 69**, 014012 (2004).
 - [15] R. N. Cahn and S. Dawson, Phys. Lett. **B 136**, 196 (1984).
 - [16] G. Altarelli, B. Mele and F. Pitolli, Nucl. Phys. **B 287**, 205 (1987).
 - [17] T. Han, G. Valencia and S. Willenbrock, Phys. Rev. Lett. **69**, 3274 (1992).

- [18] S. L. Glashow, D. V. Nanopoulos and A. Yildiz, Phys. Rev. **D 18**, 1724 (1978).
- [19] R. Kleiss, Z. Kunszt and W. J. Stirling, Phys. Lett. **B 253**, 269 (1991).
- [20] T. Han and S. Willenbrock, Phys. Lett. **B 273**, 167 (1991).
- [21] S. Dawson, S. Dittmaier and M. Spira, Phys. Rev. **D 58**, 115012 (1998).
- [22] T. Plehn, M. Spira and P. M. Zerwas, Nucl. Phys. **B 479**, 46 (1996); Nucl. Phys. **B 531**, 655(E) (1998).
- [23] A. Belyaev, M. Drees, O. J. P. Eboli, J. K. Mizukoshi and S. F. Novaes, Phys. Rev. **D 60**, 075008 (1998).
- [24] A. A. Barrientos Bendez and B. A. Kniehl, Phys. Rev. **D 64**, 035006 (2001).
- [25] Z. Kunszt, Nucl. Phys. **B 247**, 339 (1984).
- [26] W. Beenakker et al., Phys. Rev. Lett. **87**, 201805 (1984); Nucl. Phys. **B 653**, 151 (2003).
- [27] L. Reina and S. Dawson, Phys. Rev. Lett. **87**, 201804 (2001).
- [28] S. Dawson, L. H. Orr, L. Reina and D. Wackeroth, Phys. Rev. **D 67**, 071503 (2003).
- [29] E. Gabrielli, B. Mele and J. Rathsmann, Phys.Rev.**D77**, 015407 (2008), arXiv:0707.0797v2.
- [30] K. Arnold, T. Figy, B. Jager, D. Zeppenfeld, arXiv:1006.4237v1.
- [31] M. Chanowitz, M. Furman and I. Hinchliffe, Nucl. Phys. **B 159**, 225 (1979).
- [32] Z. Bern, A. De Freitas, L. Dixon and H. L. Wong, Phys. Rev. **D 66**, 085002 (2002).
- [33] I. Jack, D.R.T. Jones and K.L. Roberts, Z. Phys. **C63**, 151 (1994), arXiv:hep-ph/9401349.
- [34] M. A. Aivazis *et al.*, Phys. Rev. **D 50**, 3102 (1994).
- [35] J. C. Collins, Phys. Rev. **D 58**, 094002 (1998).
- [36] M. Kramer *et al.*, Phys. Rev. **D 62**, 096007 (2000).
- [37] D.A.Dicus and C.Kao, Phys. Rev. **D 38**, 1008 (1988) [Err.-ibid. **D 42**, 2412 (1990)].
- [38] B. A. Kniehl, Phys. Rev. **D 42**, 2253 (1990).
- [39] C. Kao, Phys. Rev. **D 46**, 4907 (1992).
- [40] L. G. Jin, C. S. Li, Q. Li, J. J. Liu, R. J. Oakes, Phys.Rev. **D71**, 095004 (2005), arXiv:hep-ph/0501279v2.
- [41] H. X. Zhu, C. S. Li, J. J. Zhang, H. Zhang, Z. Li, arXiv:0903.5047v2.
- [42] A. Denner, Fortschr. Phys. **41** 4 (1993).
- [43] G. Passarino, M. Veltman, Nucl. Phys. **B160** 151 (1979).
- [44] B. W. Harris, J. F. Owens, 10.1103/Phys.Rev.**D 65**, 094032 (2002), arXiv:hep-ph/0102128v3.
- [45] J. C. Collins, D. E. Soper and G. Sterman, Nucl. Phys. **B 261**, 104 (1985).

- [46] G. T. Bodwin, Phys. Rev. **D 31**, 2616 (1985); Phys. Rev. **D 34**, 3932 (E) (1986).
- [47] S. Frixion, Phys. Lett. **B429** 369-374 (1998), arXiv:hep-ph/9801442; F. Stockli, A. G. Holzner, G. Dissertori, JHEP 0510, 079 (2005).
- [48] E. Boos et al, [CompHEP Collaboration], CompHEP 4.4: Automatic computations from Lagrangians to events, Nucl. Instrum. Meth. A534 250 (2005) (arXiv:hep-ph/0403113).
- [49] C. Amsler *et al.* (Particle Data Group), Physics Letters **B 667**, 1 (2008).
- [50] M. Carena, D. Garcia, U. Nierste, C. E. M. Wagner, Nucl. Phys. **B 577**, 88 (2000).
- [51] W. Porod, Comput. Phys. Commun. 153 275 (2003) (arXiv:hep-ph/0301101).
- [52] B. C. Allanach *et al*, Eur. Phys. J. **C25**, 133 (2002).
- [53] M. Drees and S. P. Martin, hep-ph/9504324.
- [54] D. Stockinger, J. Phys. **G 34**, R45 (2007), hep-ph/0609168.

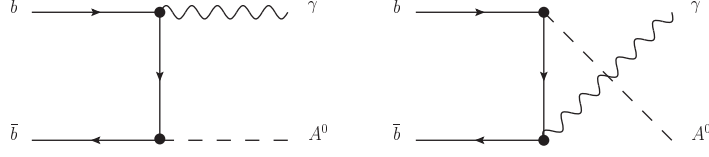


FIG. 1: Tree level Feynman diagrams for $b\bar{b} \rightarrow \gamma A^0$

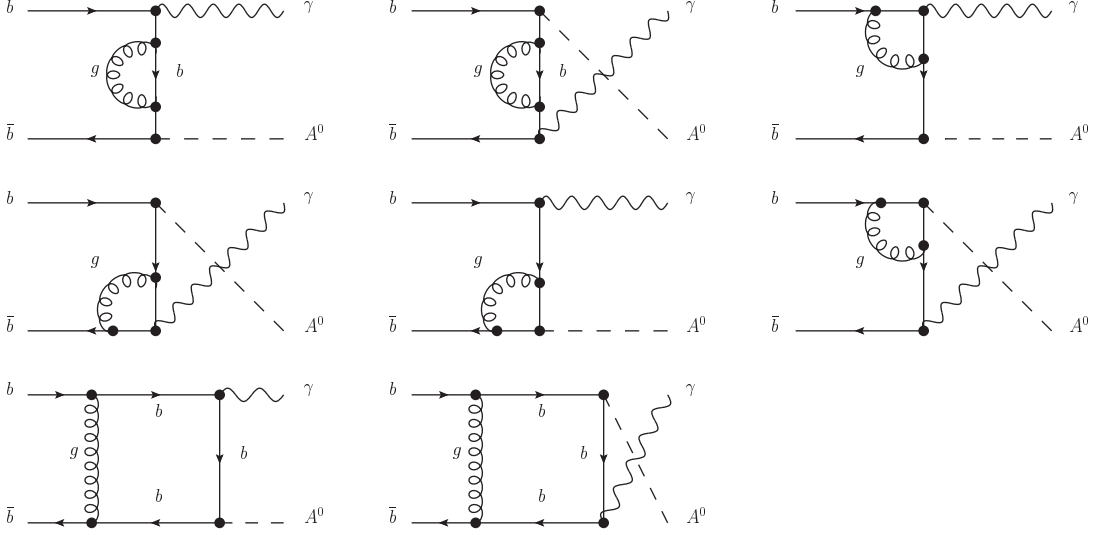


FIG. 2: The loop diagrams related to virtual gluon: propagator, vertex and box diagram corrections

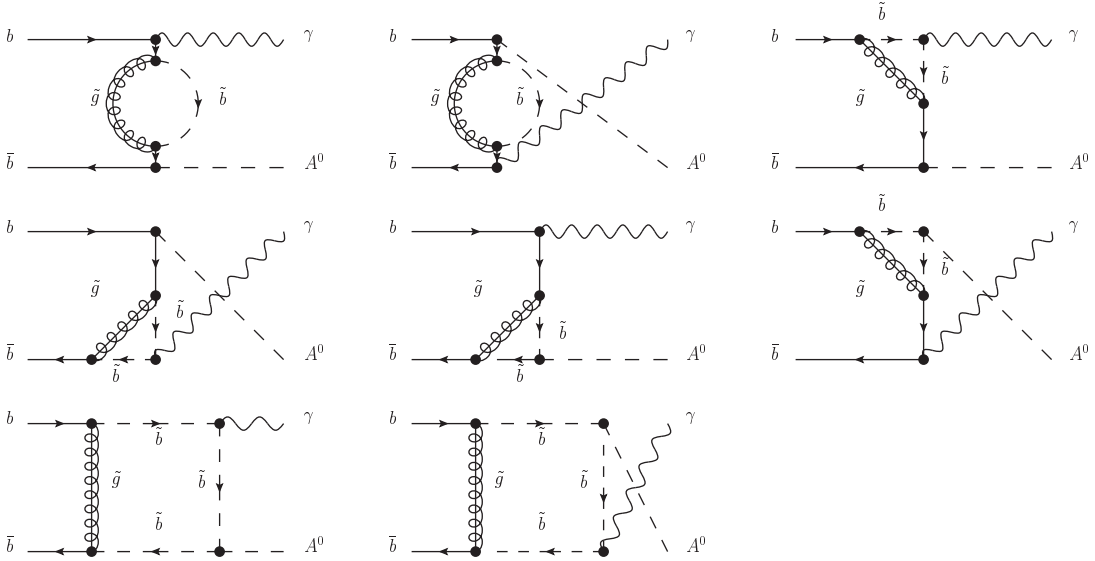


FIG. 3: The loop diagrams related to virtual gluino and sbottoms: propagator, vertex and box diagram corrections

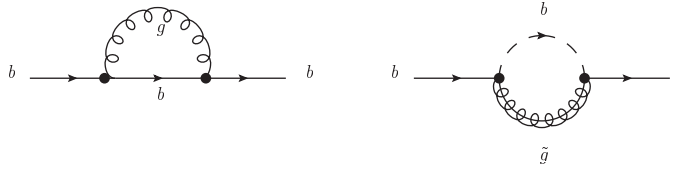


FIG. 4: Self-energy diagrams for the bottom quark

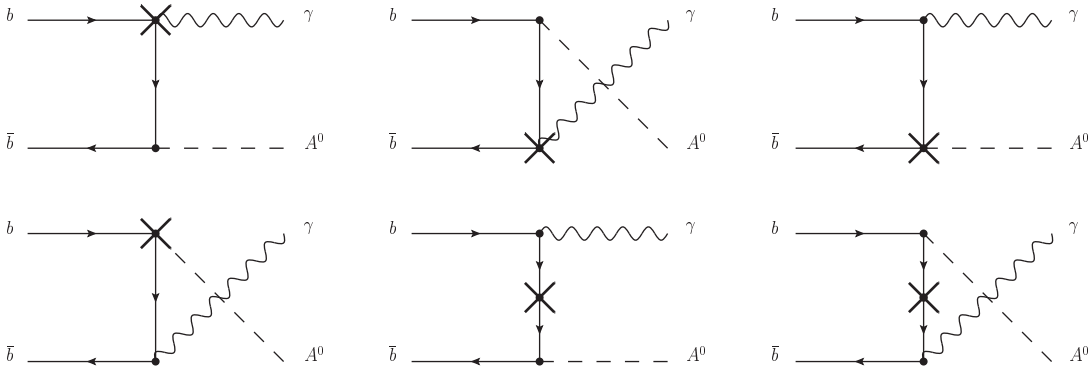


FIG. 5: Counter-term diagrams: wavefunction, mass and vertex renormalization

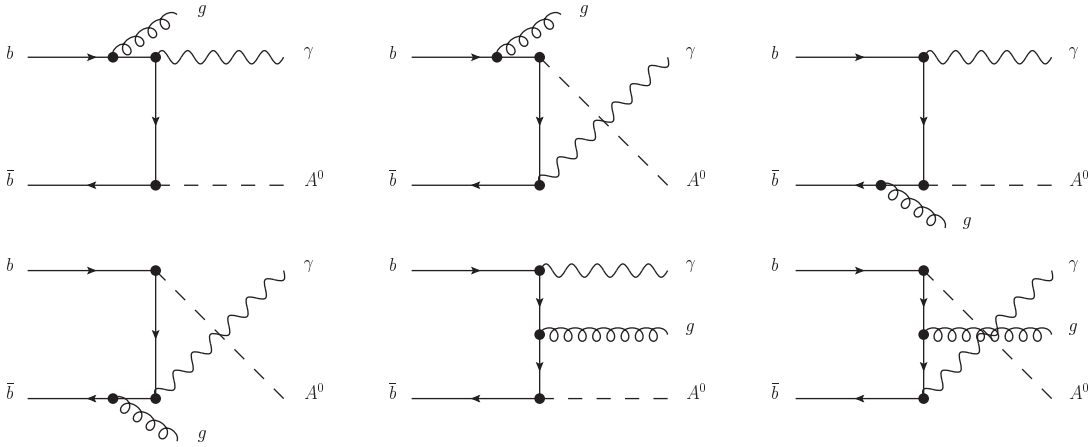


FIG. 6: Feynman diagrams for real gluon emission

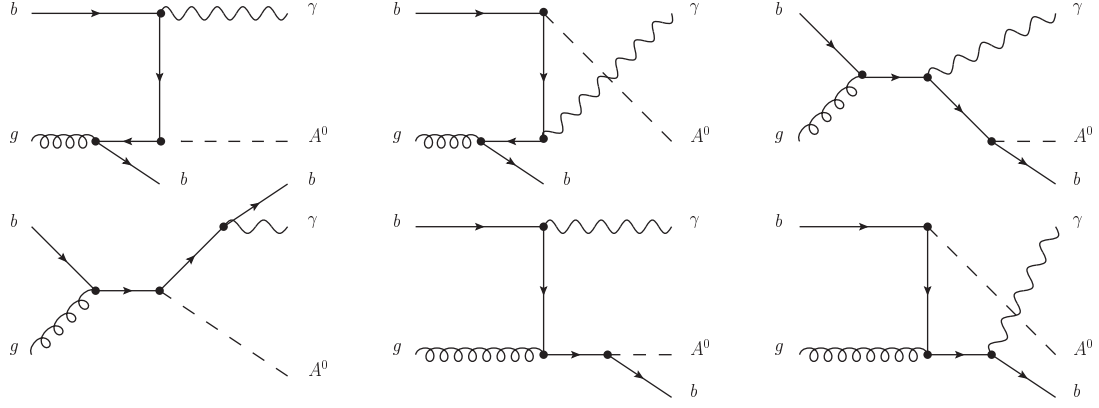


FIG. 7: Feynman diagrams for massless bottom (anti-)quark emission

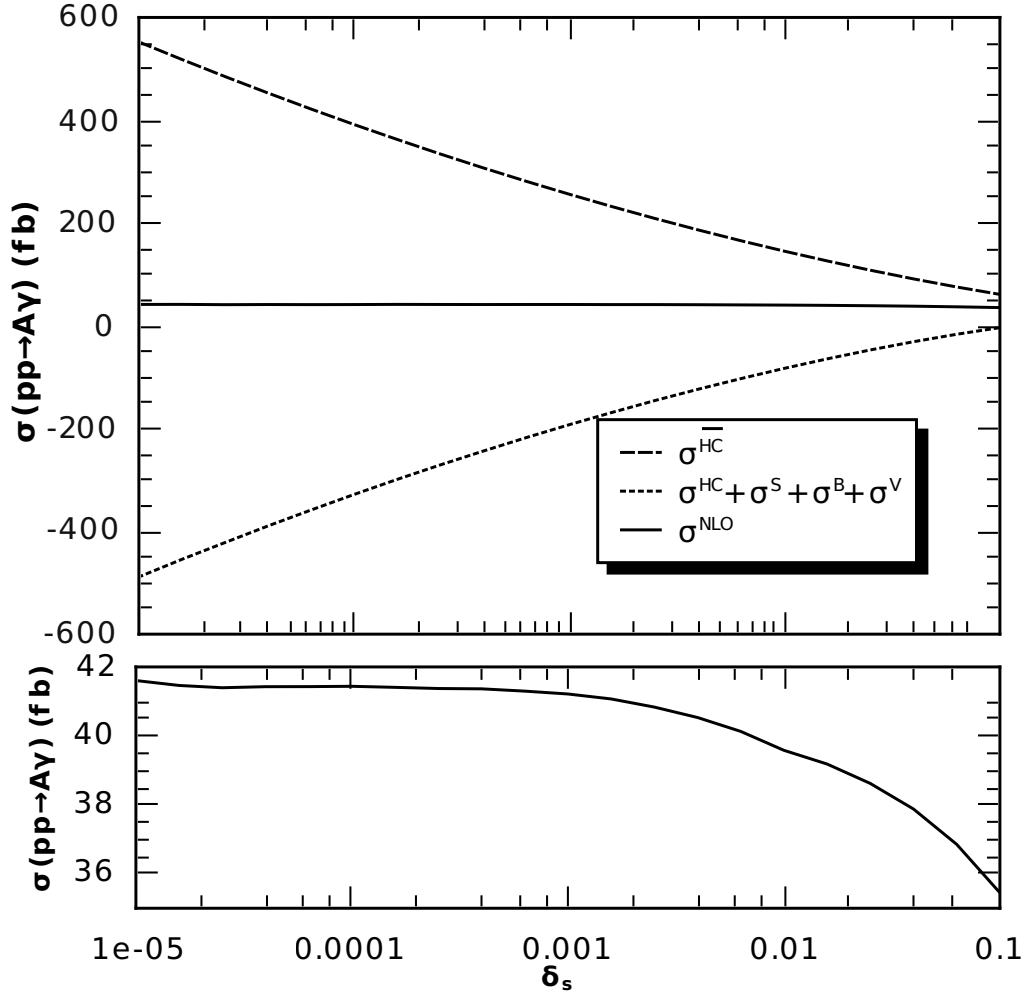


FIG. 8: Inclusive total cross sections for $pp \rightarrow A^0\gamma + X$ at the LHC as a function of δ_s in the phase space slicing treatment. Non-collinear real correction, collinear correction, soft and virtual corrections are also shown separately. The collinear cutoff is chosen to be $\delta_c = \delta_s/50$.

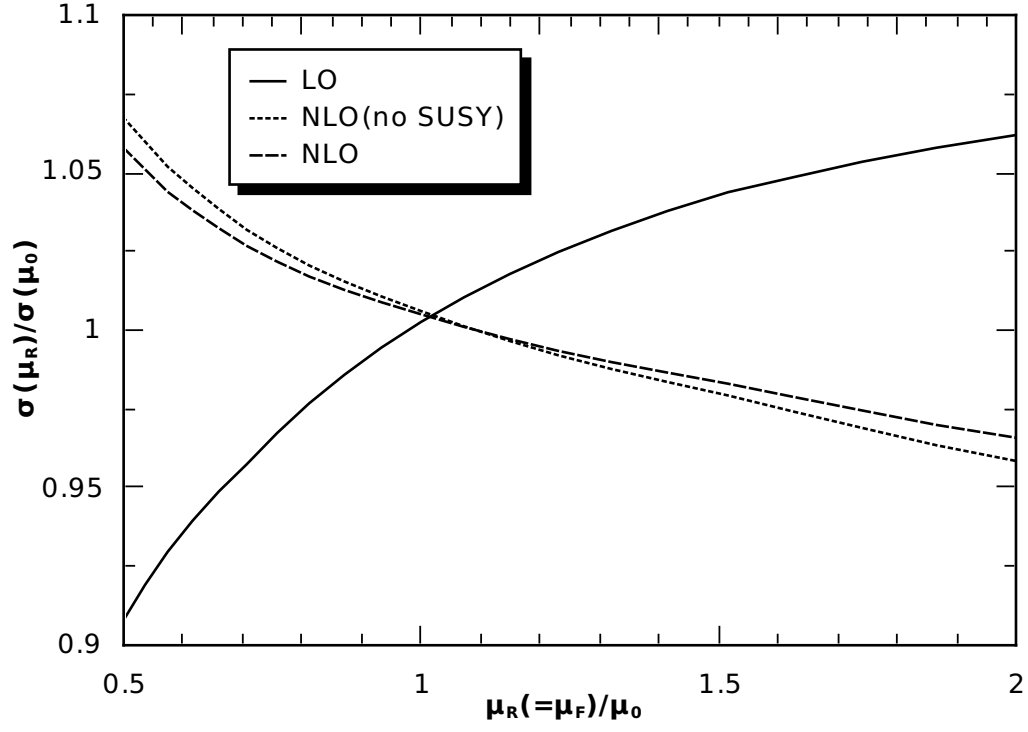


FIG. 9: Dependence of inclusive total cross section for $pp \rightarrow A^0\gamma + X$ at the LHC on the factorization scale and the renormalization scale assuming $\mu_R = \mu_F$.

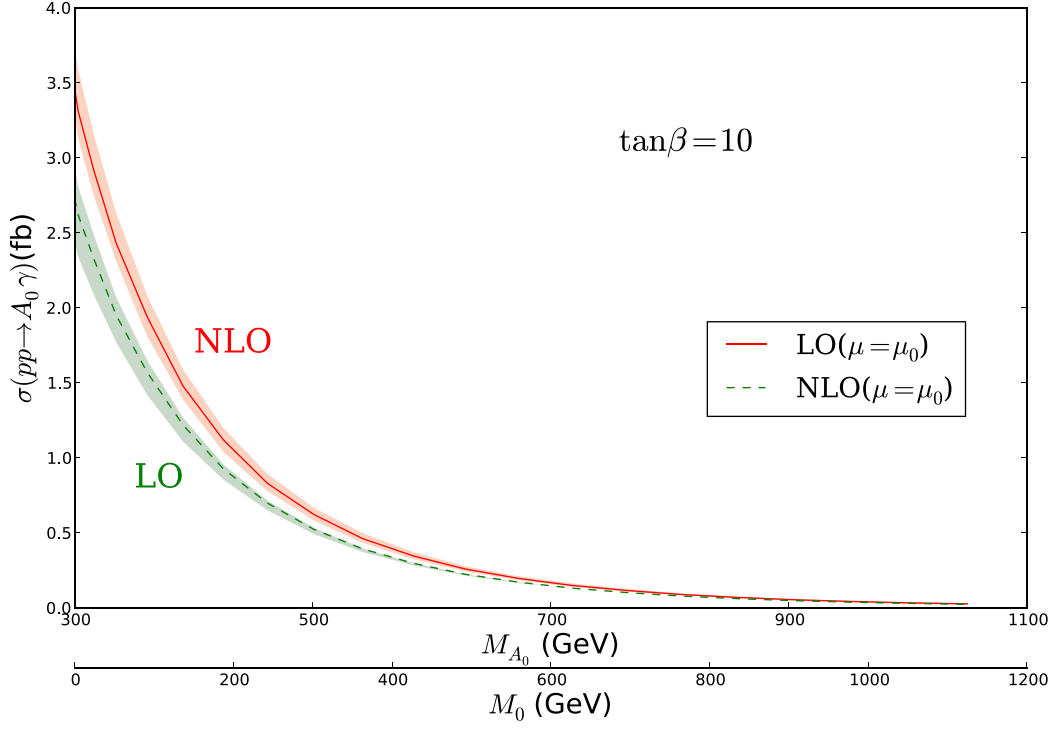


FIG. 10: The inclusive total cross sections for $pp \rightarrow A^0\gamma + X$ at the LHC as a function of m_{A^0} , with $\tan\beta = 10$. The bands are obtained by varying the renormalization and factorization scale between $\mu_R(=\mu_F) = \mu_0/2$ and $\mu_R(=\mu_F) = 2\mu_0$.

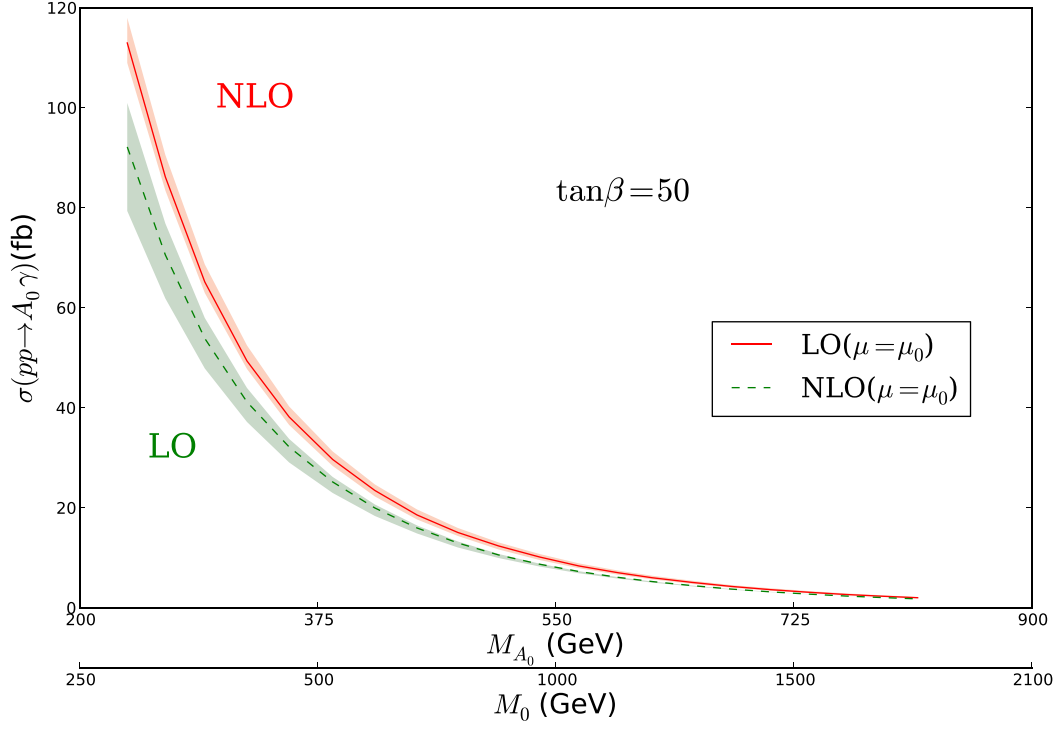


FIG. 11: The inclusive total cross sections for $pp \rightarrow A^0\gamma + X$ at the LHC as a function of m_{A^0} , with $\tan\beta = 50$. The bands are obtained by varying the renormalization and factorization scale between $\mu_R(=\mu_F) = \mu_0/2$ and $\mu_R(=\mu_F) = 2\mu_0$.

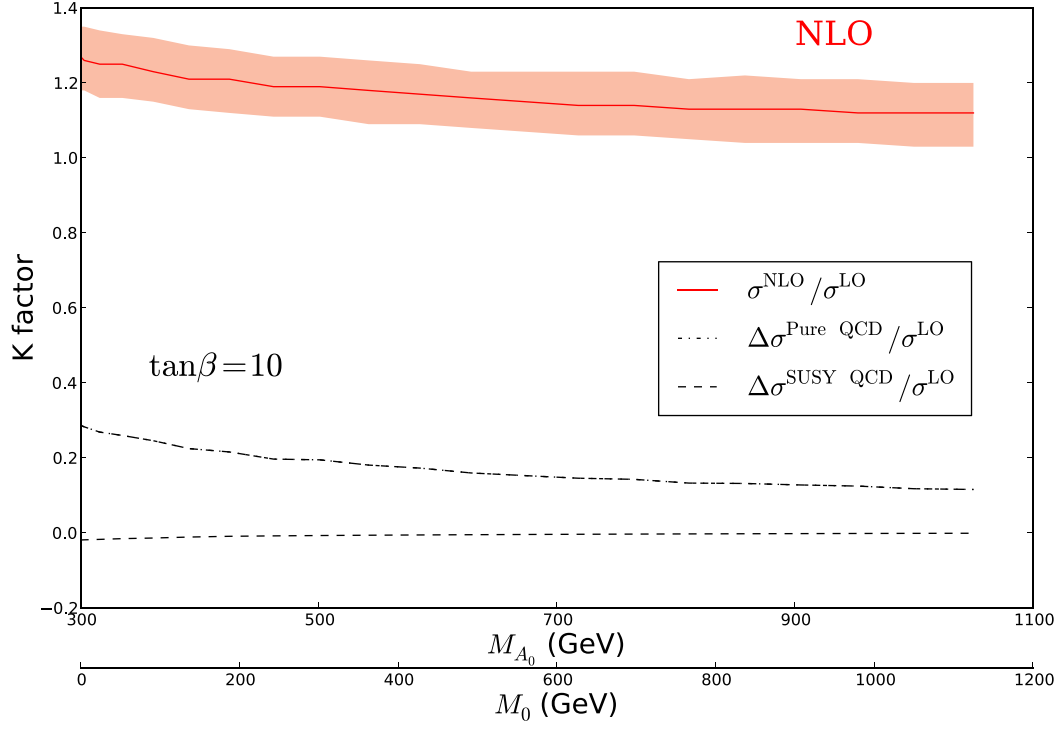


FIG. 12: K-factors for $pp \rightarrow A^0\gamma + X$ at the LHC with $\tan\beta = 10$. The band is obtained by varying the scale in the NLO calculations between $\mu_R(=\mu_F) = \mu_0/2$ and $\mu_R(=\mu_F) = 2\mu_0$.

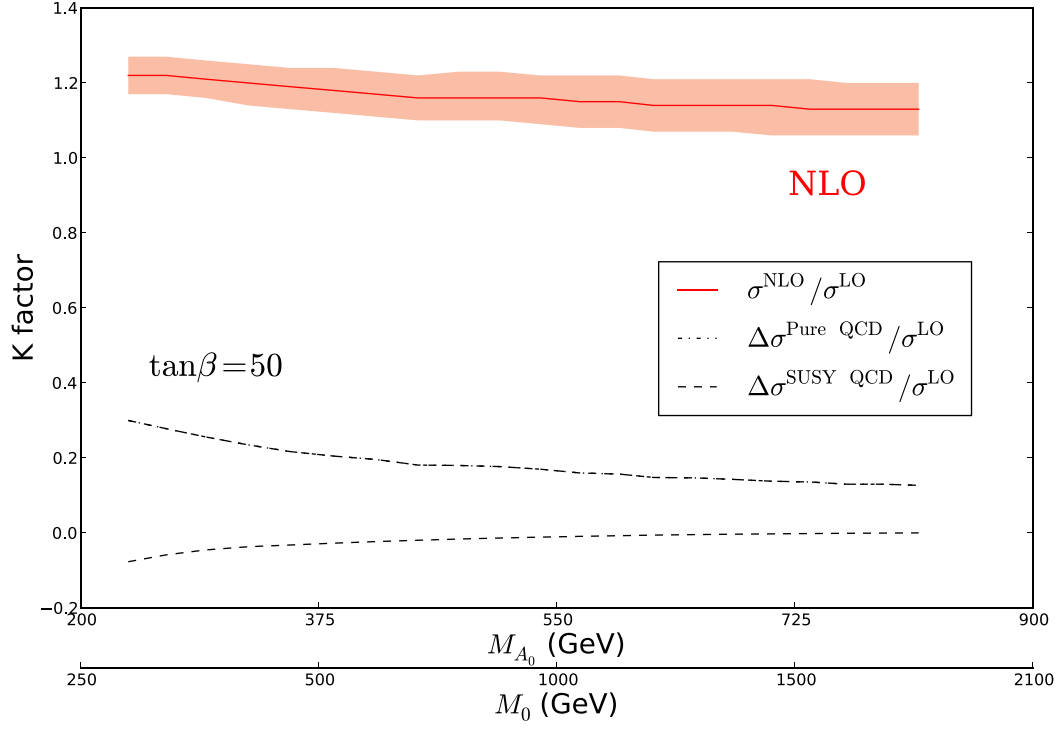


FIG. 13: K-factors for $pp \rightarrow A^0\gamma + X$ at the LHC with $\tan\beta = 50$. The band is obtained by varying the scale in the NLO calculations between $\mu_R(=\mu_F) = \mu_0/2$ and $\mu_R(=\mu_F) = 2\mu_0$.

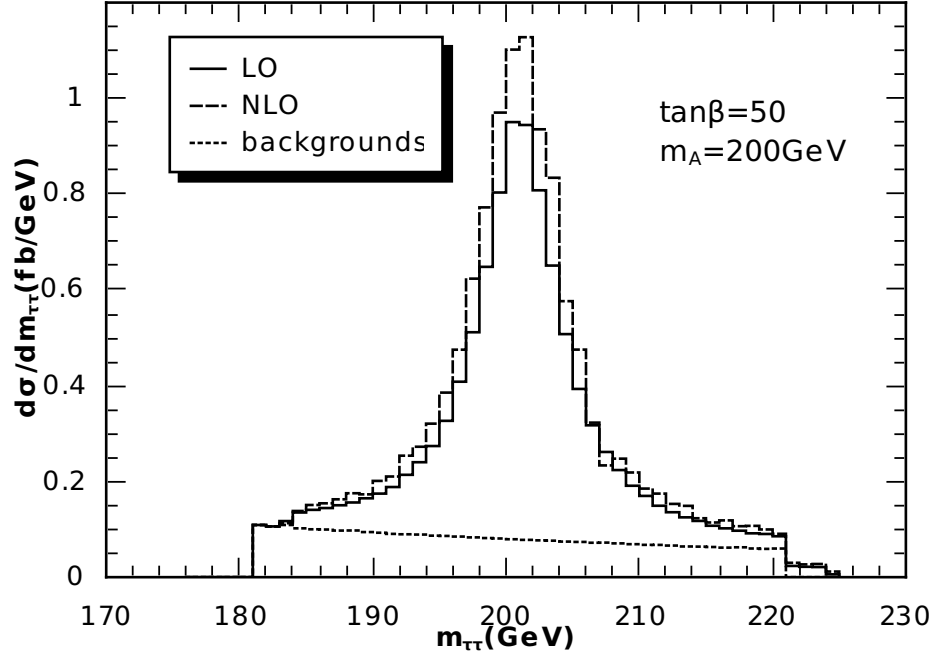


FIG. 14: Final state $\tau\tau$ invariant mass distribution for $pp \rightarrow A^0\gamma + X \rightarrow \tau^+\tau^-\gamma + X$ at the LHC compared with the background.

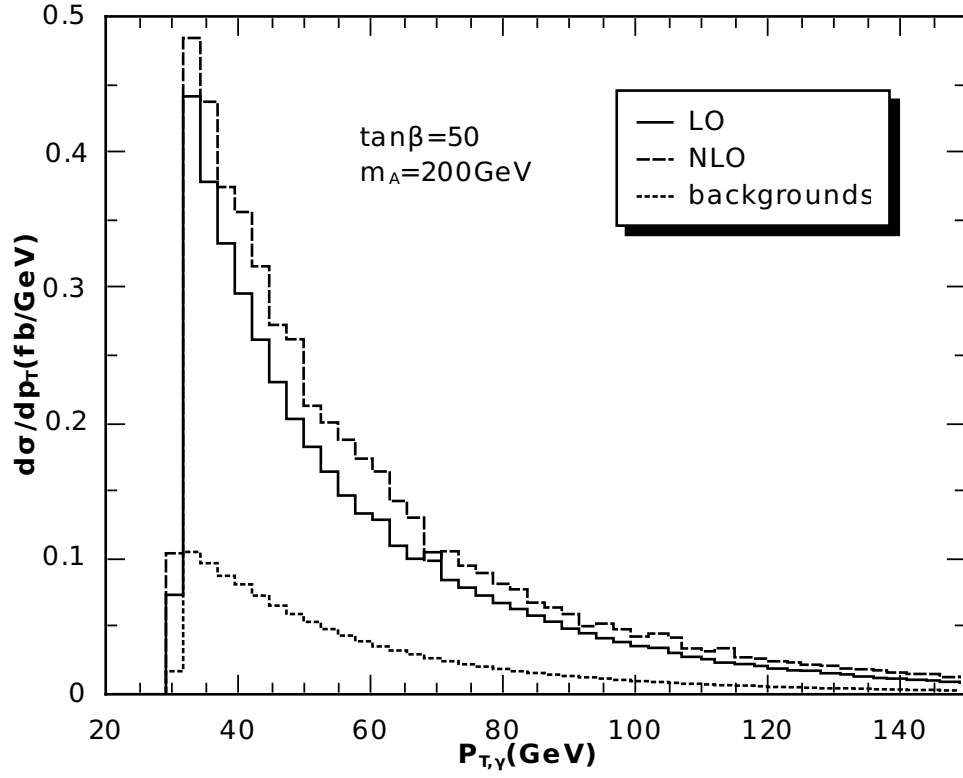


FIG. 15: The photon transverse momentum distribution for $pp \rightarrow A^0\gamma + X \rightarrow \tau^+\tau^-\gamma + X$ at the LHC as compared with the background.

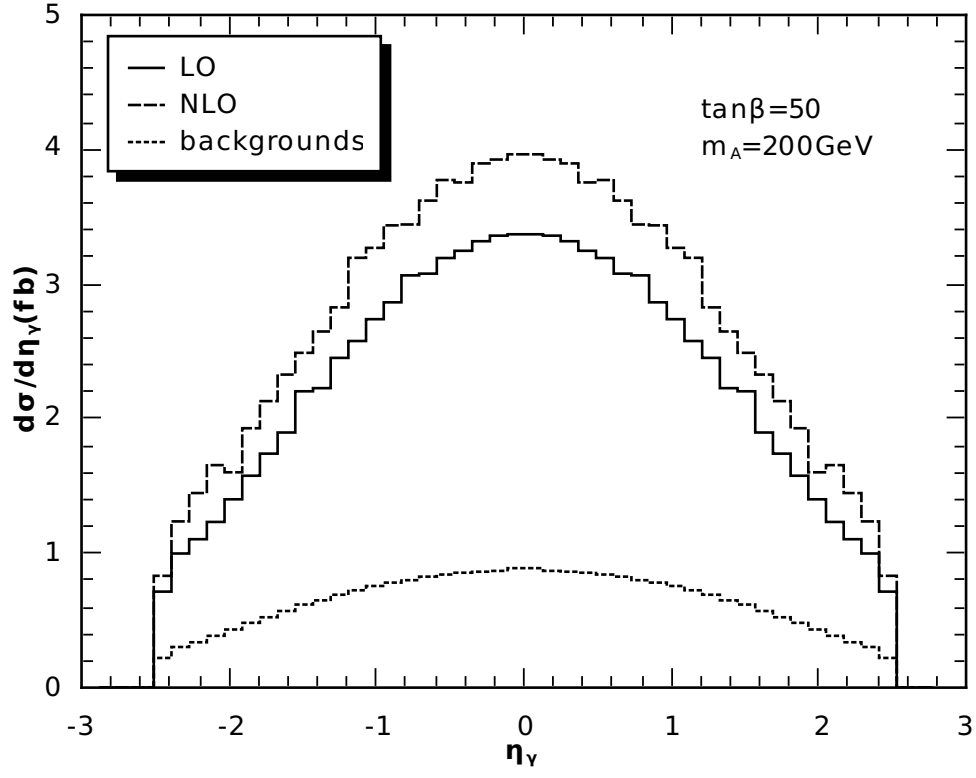


FIG. 16: Photon transverse momentum distribution for $pp \rightarrow A^0\gamma + X \rightarrow \tau^+\tau^-\gamma + X$ at the LHC as compared with the background.